



Cite this: *New J. Chem.*, 2021, 45, 8283

Carbon dioxide hydrogenation to methanol over polybenzoxazine-based mesocarbon supported Cu–Zn catalyst†

Varisara Deerattrakul,^a Anurak Chukchuan,^a Nattanida Thepphankulngarm,^a Jirayu Pornjaturawit,^a Napas Vacharameteavoranun,^a Thanyalak Chaisuwan^{bc} and Paisan Kongkachuichay^{id}*^a

Carbonaceous material has been generally recognized as a stable and functionalized catalyst support and has a high surface area. It has been reported that the nitrogen species can enhance metal dispersion, leading to a promising catalytic activity. To achieve this goal, a high-surface-area carbon material, so-called “mesocarbon”, was synthesized *via* carbonization of polybenzoxazine (PBZ). The 15% CuZn/mesocarbon catalyst was prepared by an incipient wetness impregnation with equimolar concentrations of Cu and Zn and then its applicability in the direct methanol synthesis from CO₂ hydrogenation was tested. It was found that 15% CuZn/mesocarbon catalyst exhibited the highest methanol productivity (498 mg g_{cat}^{−1} h^{−1}) and CO₂ conversion (28 ± 2%) at a reaction temperature and pressure of 240 °C and 15 bar, respectively. These high catalytic properties can be assigned to the high surface area of mesocarbon (up to 471 m² g^{−1}) and high nitrogen content (2.31%), which can prevent metal agglomeration and improve hydrogen dissociation.

Received 25th March 2021,
Accepted 19th April 2021

DOI: 10.1039/d1nj01475g

rsc.li/njc

1. Introduction

Rising emissions of carbon dioxide (CO₂) into the atmosphere together with the rapid growth of the economy have become of growing concern for the environment, with problems mainly originating from the combustion of fossil fuels and leading to consequences for global climate change such as ocean acidification and sea-level rise, among others.¹ To date, carbon capture and storage (CCS) technologies have been widely used as efficient solutions to reduce CO₂ emissions, *via* the absorption and mineralization of CO₂ over liquids and solids.² However, there are many limitations to these technologies, such as process costs, corrosion problems, and the implementation of large-scale use.^{3,4} Therefore, instead of using technologies with such limitations, converting CO₂ through the CO₂ hydrogenation process or electrocatalytic reduction of CO₂ into value-added

products, especially methanol, is a potential profitable strategy that not only reuses CO₂ from emissions but also responds to the demands of sustainable development.^{5–8} It is well-known that methanol is a key chemical platform, which can be directly used as a sustainable synthetic fuel and precursor for higher-hydrocarbon production (*e.g.* aromatics, biodiesel, formaldehyde, and olefins).^{9–13} Methanol synthesis *via* CO₂ hydrogenation is an exothermic reaction, therefore the thermodynamics of the reaction favors methanol formation at high pressure and low temperature.¹⁴ Typically, operation at an industrial scale uses a pressure from 5 MPa to 10 MPa and temperature from 200 °C to 300 °C over a Cu/ZnO/Al₂O₃ catalyst.^{15,16}

In general, Cu/ZnO-based catalysts are widely used as efficient catalysts to synthesize methanol from CO₂ hydrogenation reaction, and the catalytic activity depends on the exposed area of Cu.^{17–19} Thus, it is vital to develop an appropriate design of the catalysts so as to improve the catalytic performance of CO₂ hydrogenation to methanol. There has been much effort put into creating high efficiency and good stability of such catalytic systems. Arena *et al.*²⁰ synthesized Al₂O₃, CeO₂, and ZrO₂ supported Cu–Zn catalysts and found that the oxide carrier can control the texture and adsorption properties of the Cu–ZnO, which affects the catalytic activity. An *et al.*²¹ introduced metal–organic frameworks (MOFs) to anchor the Cu/ZnO_x, leading to the prevention of agglomeration of Cu–Zn and of phase separation between Cu and ZnO_x, as well as to obtain

^a Department of Chemical Engineering, Faculty of Engineering, and Research Network of NANOTEC-KU on NanoCatalysts and NanoMaterials Sustainable Energy and Environment, Kasetsart University, Bangkok 10900, Thailand. E-mail: jengpsk@ku.ac.th; Fax: +66 2561 4621; Tel: +66 2797 0999 ext. 1207

^b The Petroleum and Petrochemical College, Chulalongkorn University, Bangkok 10330, Thailand

^c Center of Excellence on Petrochemical and Materials Technology, Bangkok 10330, Thailand

† Electronic supplementary information (ESI) available: XRD pattern of spent catalyst. See DOI: 10.1039/d1nj01475g

ultrafine Cu/ZnO_x nanoparticles. Moreover, carbon nanotubes,²² graphene nanosheets,²³ and graphene aerogel²⁴ are able to improve the Cu–Zn dispersion and inhibit Cu–Zn sintering, leading to enhancement of the catalytic performance.

Polybenzoxazine (PBZ) has attracted attention due to its unique properties such as low moisture absorption, molecular design flexibility, good thermal and chemical stability, near-zero volume shrinkage upon curing, and both catalysts and by-products being free upon ring-opening polymerization.^{25–27} Additionally, the nitrogen atoms on PBZ can be transformed to electroactive nitrogen functionalities during one-step carbonization, which provides an important key for promoting methanol production.²⁸ There are some studies dealing with the CO₂ adsorption by nitrogen-functionalized carbon materials. They reported that the nitrogen functional groups can enhance the adsorptive properties of carbon material leading to high CO₂ capture performance.^{29–31} Compare to reduced graphene oxide aerogel, PBZ-based mesocarbon can be prepared with a lower-cost and environmental-friendly process.³²

In this work, PBZ-based mesocarbon support with nitrogen-enriched porous carbon was facile synthesized by using benzoxazine solventless method under ambient-pressure drying. Subsequently, self-formation of the mesopore structure occurred during the sol–gel process without applying an external ultrasonic irradiation or a hard template, and then this mesoporous structure was transformed to mesoporous carbon by carbonization process. To the best of our knowledge, PBZ-based mesocarbon support has not yet been reported for use as a support for Cu–Zn catalyst in CO₂ hydrogenation to methanol. Understanding the PBZ-based mesocarbon support, which is an effective material in terms of environment-friendliness, low production cost, and high methanol productivity will lead to further improvement of related carbon materials for CO₂ hydrogenation reaction.

2. Experimental

2.1 Chemicals and materials

The chemicals used in this study without further purification were phenol in detached crystal (99.99% C₆H₆O, Fisher Scientific), paraformaldehyde (95%, Sigma Aldrich), ethylenediamine (99% C₂H₈N₂, Sigma Aldrich), dimethylformamide (99.8% C₃H₇NO, Labscan Asia Co.), acetone (C₃H₆O, QRec), copper nitrate trihydrate (99.5% Cu(NO₃)₂·3H₂O, QRec), zinc nitrate hexahydrate (98% Zn(NO₃)₂·6H₂O, Lobachemie), and water purified by using a Milli-Q system (> 18 MΩ cm, Millipore).

2.2 Synthesis of polybenzoxazine-based mesocarbon xerogel

Firstly, PBZ was synthesized by the solventless method described by the Ishida *et al.*³³ Briefly, benzoxazine precursor was synthesized using reagents in a mole ratio of 2:4:1 phenol (9.4110 g):paraformaldehyde (6.3220 g):ethylenediamine (3.0355 g) under stirring at 110 °C for approximately 60 min until a transparent yellow mixture was obtained. Next, the as-synthesized monomer was dissolved into dimethylformamide

up to a concentration of 30 wt%, then sealed off in a glass vial, and left for 90 min at 150 °C in an oil bath to form PBZ gels. These PBZ gels were cut into a cubic block and immersed in acetone, which was then renewed every 12 h for the next two days, before being dried at 80 °C for 12 h. PBZ xerogels were obtained and then cured in an oven for step polymerization at 160 °C, 180 °C, 190 °C, 210 °C, and 220 °C for 1, 2, 6, 3, and 0.5 h, respectively, to achieve a fully cured polybenzoxazine xerogel with high porosity. Subsequently, the as-synthesized material was pyrolyzed under a nitrogen flow of 600 cm³ min^{−1} following four steps: (1) 35–200 °C for 1 h, (2) 200–600 °C for 6 h, (3) 600–800 °C for 2 h, and finally (4) held at 800 °C for 2 h. After cooling to room temperature under nitrogen atmosphere, PBZ-based mesocarbon xerogel was finally obtained.

2.3 Synthesis of Cu–Zn/mesocarbon catalyst

The 15 wt% of Cu–Zn-loaded mesocarbon catalyst was synthesized by incipient wetness impregnation method with an equimolar concentration of Cu and Zn. First mixed solution of Cu(NO₃)₂ and Zn(NO₃)₂ was prepared, and then it was dropped into PBZ-based mesocarbon xerogel with proper amount corresponding to the void volume of the support. After stirring for 15 min, the as-prepared catalyst was then dried at 100 °C for 12 h and calcined in air at 350 °C with a heating rate of 2 °C min^{−1} for 2 h to remove impurities and form metal oxides (*i.e.*, CuO and ZnO).³⁴

2.4 Characterization of catalysts

Fourier transform infrared (FTIR) spectra of the samples were obtained using a Fourier transform infrared spectrometer (Bruker TENSOR 27) equipped with a DTGs detector in the 400–4000 cm^{−1} range with a resolution of 4 cm^{−1}. The morphology of the samples was analyzed by a field-emission scanning electron microscope (FE-SEM: JEOL, JSM-7600F) equipped with energy-dispersive X-ray spectroscopy (EDS), operating at 5 kV with Pt coating of the sample (thickness of *ca.* 2 nm), and a transmission electron microscope (TEM; JEOL JEM-3100F) operating at 300 kV. Note that the samples were dispersed in ethanol solution by sonication and then dried at room temperature on copper grids with a 200 mesh. X-Ray diffraction (XRD) patterns were recorded by a Bruker D8 Advance diffractometer using Cu-K_α radiation ($\lambda = 1.54 \text{ \AA}$) at 40 kV and 30 mA in the 2θ range from 5° to 90° with a step size of 0.02° and a time per step of 115 s. N₂ adsorption–desorption isotherms of samples were obtained by using a Quantachrome Autosorb-1C analyzer at −196 °C, and samples were degassed at 100 °C for 12 h before the measurement. The specific surface areas of as-synthesized samples were determined by the Brunauer–Emmett–Teller (BET) method over the relative pressure (P/P_0) of 0.05–0.3, and their pore size distribution were calculated by the Barrett–Joyner–Halenda (BJC) method using obtained adsorption isotherms. The structural characterization of carbon materials was investigated by Raman spectroscopy using a Senterra Dispersive Raman Microscope (Bruker Optics) at 532 nm with an excitation power of 20 mw. To determine the thermal stability and decomposition of the as-synthesized samples, a thermogravimetric analyzer (TGA: PerkinElmer) was used under flowing

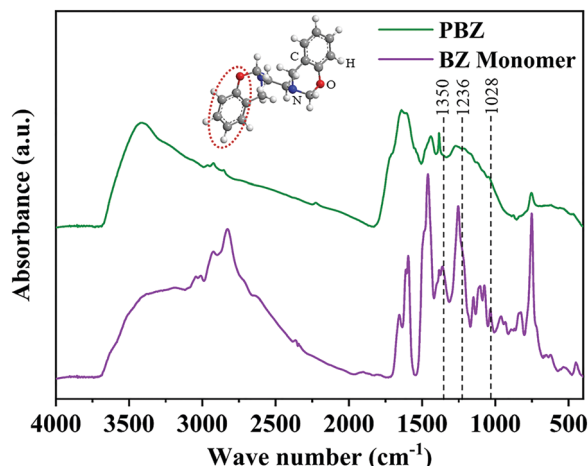


Fig. 1 FTIR spectra of BZ monomer and polybenzoxazine.

of air (100 mL min^{-1}) from 25 to 800°C with a heating rate of $10^\circ\text{C min}^{-1}$. X-Ray photoelectron spectroscopy (XPS) was performed with an AXIS Ultra DLD spectrometer (Kratos Analytical Ltd) using the monochromatic Al K_{α} X-ray source of 1486.6 eV to identify the surface chemical compositions. Reduction properties were investigated by temperature-programmed reduction (TPR) using a continuous-flow tubular fixed-bed reactor equipped with a thermal conductivity detector (TCD). Briefly, 0.10 g catalyst was packed in a quartz tube and heated under a flowing gas mixture of $10\% \text{ H}_2$ in Ar (30 mL min^{-1}) at a heating rate of 5°C min^{-1} in a temperature range from 50 to 1000°C .

2.5 Catalytic reaction test

The catalytic activity of the as-synthesized catalyst when used for CO_2 hydrogenation to methanol was evaluated *via* a tubular stainless steel fixed-bed reactor. Firstly, 0.40 g of catalyst was *in situ* reduced with H_2 (40 mL min^{-1}) under atmospheric pressure at 350°C for 90 min and then cooled down to room temperature. Subsequently, a flow of H_2 and CO_2 mixture ($\text{H}_2:\text{CO}_2$ molar ratio of $3:1$) at a gas hourly space velocity (GHSV) of 2444 h^{-1} was fed through the reactor, and the activity was examined at a pressure of 15 bar and various reaction temperatures. Finally, the obtained product was analyzed by an online chromatograph (Shimadzu GC-14A) equipped with a flame ionization detector (FID) in a Porapak-Q column and a thermal conductivity detector (TCD) in a Unibead-C column. Moreover, the space-time yield of methanol ($\text{mg g}_{\text{cat}}^{-1} \text{ h}^{-1}$) was calculated as follows:

$$\text{space-time yield of methanol} = \frac{\text{moles methanol}}{\text{amount of catalyst} \times V_{\text{sampling}}} \times \dot{V}_{\text{total}} \times \text{MW}_{\text{methanol}} \quad (1)$$

where $\text{MW}_{\text{methanol}}$ is the molecular weight of methanol (32 g mol^{-1}); V_{sampling} and \dot{V}_{total} are the volume of sampling for gas chromatography and the total volumetric flow of H_2 and CO_2 mixtures, respectively.

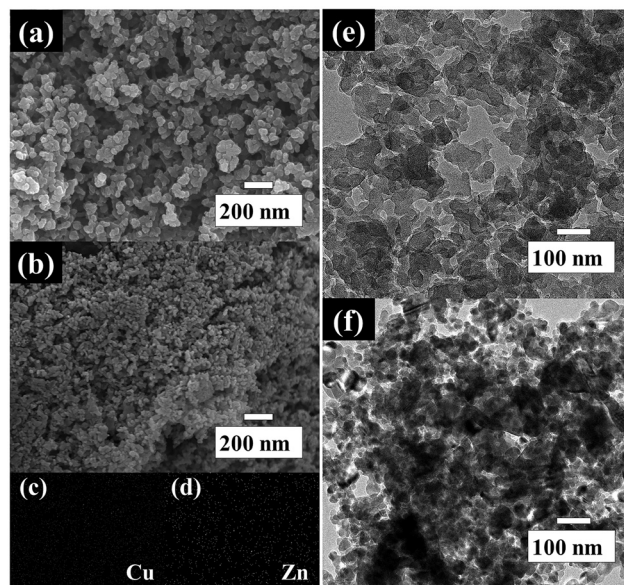


Fig. 2 FE-SEM images of (a) mesocarbon and (b) 15% CuZn/mesocarbon, with EDS mapping of 15% CuZn/mesocarbon showing (c) Cu and (d) Zn; and TEM images of (e) mesocarbon and (f) 15% CuZn/mesocarbon.

3. Results and discussion

The formation of benzoxazine (BZ) monomer was confirmed by FTIR. The presence of peaks at 1028 cm^{-1} and 1236 cm^{-1} can be assigned to the asymmetric stretching of Ph-O-C groups,³⁵ while the peak at 1350 cm^{-1} is associated with the CH_2 wagging of oxazine.³⁶ Additionally, it can be noticed that the characteristic peaks of BZ monomer disappeared after polymerization, indicating the successful formation of PBZ as shown in Fig. 1.

The morphologies of all samples are shown in Fig. 2. As can be seen in the FE-SEM images of mesocarbon (Fig. 2a) and the 15% CuZn/mesocarbon catalyst (Fig. 2b), the mesocarbon support shows a three-dimensional interconnected network of carbon particles with a size of *ca.* 30 nm and irregular coral-like particles on top, while the catalyst displays good dispersion of small spherical particles of CuO-ZnO with a size of *ca.* 10 nm over mesocarbon support, which is confirmed by EDX mapping results (Fig. 2c and d). The observed size of bimetallic particles is in good agreement with our previous work.³⁷ The TEM image of mesocarbon (Fig. 2e) exhibits a uniformly interconnected structure of large pores. Fig. 2f presents the TEM image of the catalyst; the surface of mesocarbon coated with Cu-Zn nanoparticles can be clearly observed, which is consistent with the FE-SEM result.

Fig. 3a presents the XRD patterns of pristine mesocarbon support and the catalyst. The support shows a single peak at around $2\theta = 43^\circ$, which is assigned to diffraction from the (100) plane,³⁸ whereas the CuZn/Mesocarbon catalyst shows peaks confirming the formation of metal oxides.^{23,24} Pore characteristics of all samples investigated by N_2 sorption technique are shown in Fig. 3b. The N_2 isotherms of all samples can be classified as a combination of type IIb with H3 hysteresis loop and type Ic, indicating a microporous adsorbent containing

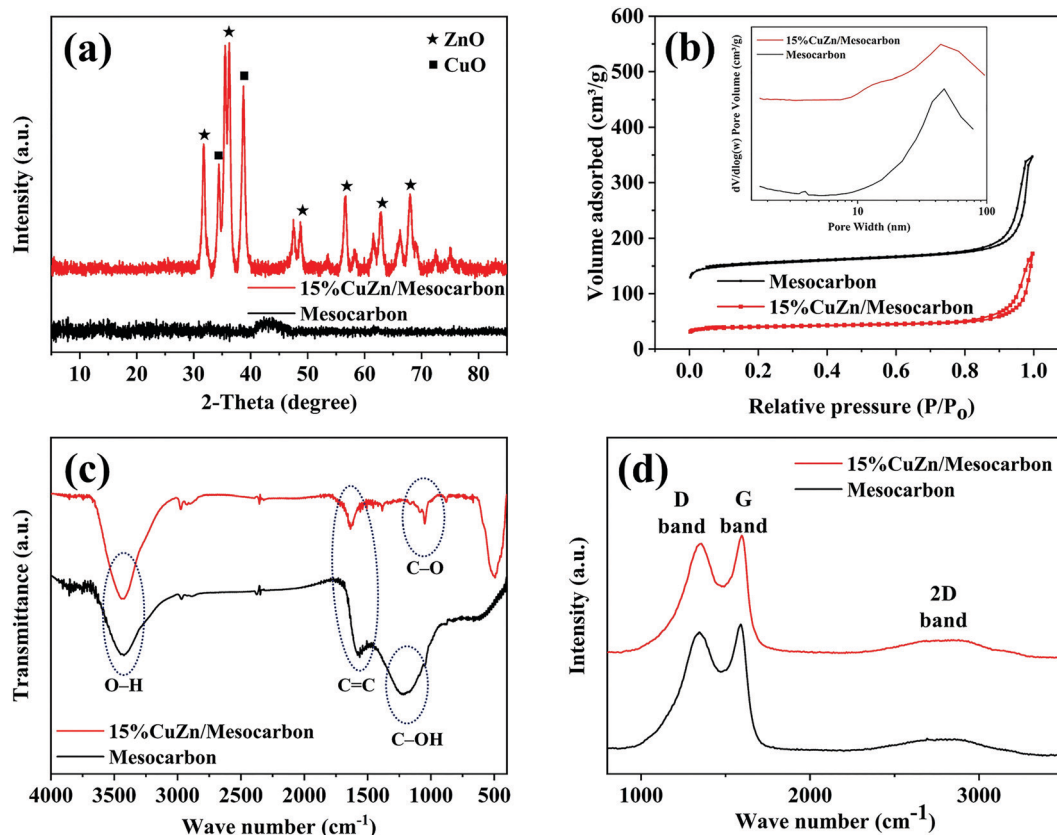


Fig. 3 (a) XRD patterns, (b) N_2 sorption isotherms, (c) FTIR spectra, and (d) Raman spectra of mesocarbon and 15% CuZn/mesocarbon.

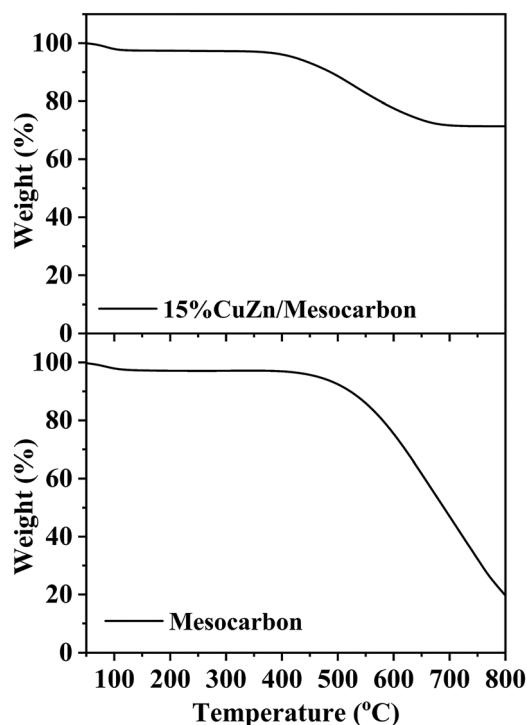


Fig. 4 TGA curves of mesocarbon and 15% CuZn/mesocarbon.

mesopores and macroporous adsorbent, respectively.³⁹ Moreover, the BET surface area and average pore diameter of mesocarbon support were found to be $471 \text{ m}^2 \text{ g}^{-1}$ and 47 nm, respectively. After loading Cu-Zn metals, the catalyst exhibited a BET surface area of $126 \text{ m}^2 \text{ g}^{-1}$ and average pore diameter of 44 nm. A decrease in BET surface area is typically observed when loading with metals on the support.^{40,41} Additionally, all samples show a pore size distribution in the range of 10–50 nm, confirming the mesoporous structure (see the inset of Fig. 3b). FTIR spectra of mesocarbon support and the catalyst were recorded to demonstrate the functional groups, as shown in Fig. 3c. The peak at 3423 cm^{-1} is associated with O–H stretching on the surface of samples and water absorption. The other peaks at around 1597 cm^{-1} , 1219 cm^{-1} , and 1049 cm^{-1} are owing to C=C, C–OH, and C–O stretching, respectively.⁴² The Raman spectra in Fig. 3d display two dominant peaks, at 1347 cm^{-1} (D band) and 1589 cm^{-1} (G band), assigned to the vibration of sp^3 disordered carbon atoms and sp^2 ordered carbon atoms, respectively. Additionally, the minor peak at around 2713 cm^{-1} (2D band) indicates a highly ordered graphitic lattice and a structural defect due to the substitution of nitrogen atoms in the carbon structure.^{43–45}

To define the thermal properties of mesocarbon support and the catalyst, TGA curves were determined. The curves in Fig. 4 show two stages of weight loss. The first loss at around 100°C can be ascribed to the evaporation of adsorbed moisture and

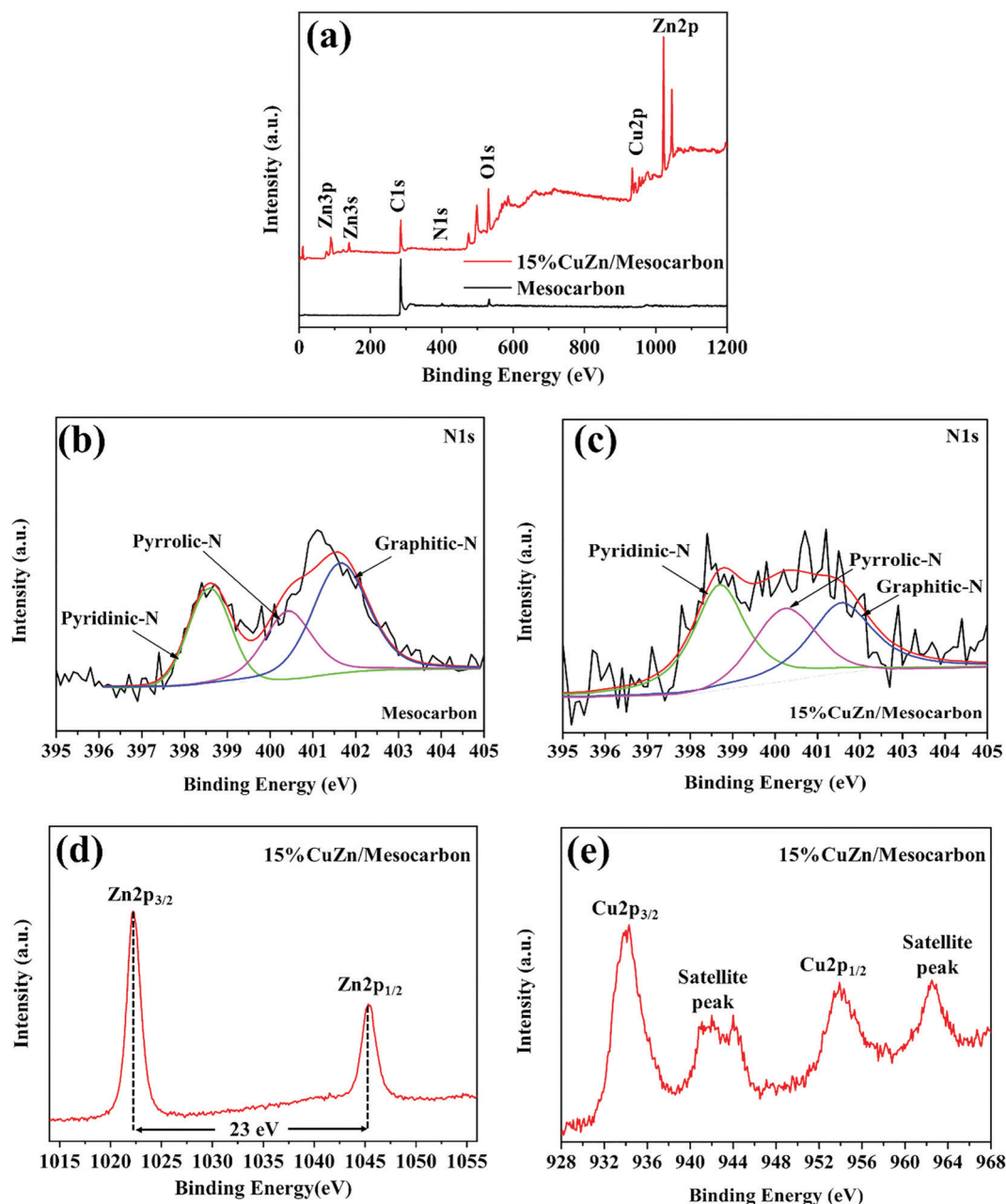


Fig. 5 XPS spectra for (a) survey spectra, (b and c) N1s (d) Zn2p, and (e) Cu2p of the as-prepared samples.

other impurities. The subsequent major loss above 450 °C is probably due to the degradation of carbon structure. It was found that the weight percentage of the remaining ash in the catalyst is about 70%, compared to 20% in the pristine mesocarbon.

XPS analysis of the catalyst and the support was performed to study the surface elemental composition, as shown in Fig. 5. Only the C1s peak at 285.1 eV, N1s peak at 402.1 eV, and O1s peak at 532.1 eV can be identified for mesocarbon support.^{46,47} After Cu–Zn metal impregnation, the pattern shows the peaks of Cu and Zn (Fig. 5a).⁴⁸ The results clearly confirm that there are no impurities on the support and catalyst. Meanwhile, the XPS N1s spectra of mesocarbon support (Fig. 5b) and the

catalyst (Fig. 5c) can be deconvoluted into three sub-peaks – “pyridinic-N” at 398.6 eV, “pyrrolic-N” at 400.2 eV, and “graphitic-N” at 401.6 eV – and provided atomic percentages of nitrogen in the mesocarbon support and the catalyst of about 2.32 at% and 2.05 at%, respectively.⁴⁹ It can be clearly seen that after loading the Cu–Zn metals, the surface nitrogen content decreased; this is due to the fact that metals may hinder the nitrogen anchoring process or remove the nitrogen from the carbon structure.⁵⁰ The amounts of pyridinic-N, pyrrolic-N, and graphitic-N on the support and the catalyst are summarized in Table 1. Generally, pyridinic-N and pyrrolic-N are always bonded with carbon atoms, forming hexagonal and pentagonal rings, respectively, while graphitic-N is substituted for carbon

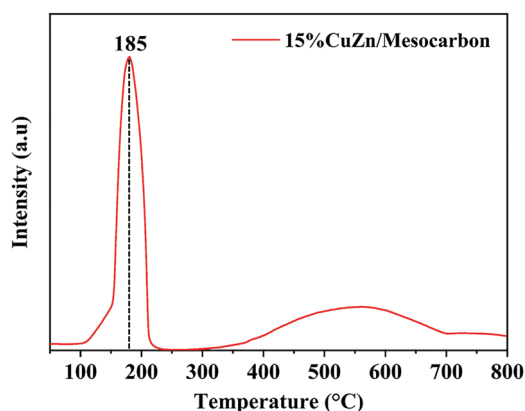
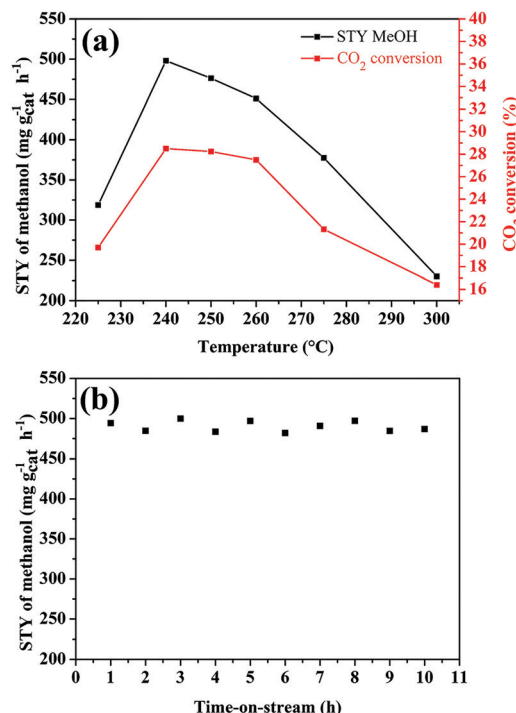
Table 1 Amounts of nitrogen species on the mesocarbon support and the catalyst

Sample	Pyridinic-N (at%)	Pyrrolic-N (at%)	Graphitic-N (at%)
Mesocarbon	0.63	0.61	1.08
15% CuZn/mesocarbon	0.84	0.54	0.67

atoms inside a hexagonal ring. Note that the nitrogen-containing groups on mesocarbon support can provide multiple electrons and also promote the formation of metal complex, leading to enhancement in the methanol productivity.^{37,51} In addition, nitrogen atoms were found to be the active sites for CO₂ capture and have a lone pair of electrons, which can donate to an electrophilic site of CO₂ molecule to the carbamate formation.⁵² The XPS spectrum of the Zn2p region of the catalyst (Fig. 5d) shows that the peaks observed at 1022.3 eV and 1045.3 eV, which are assigned to Zn2p_{3/2} and Zn2p_{1/2}, respectively, and exhibit the spin-orbit splitting of 23 eV, which can be attributed to a completely oxidized state of ZnO.⁵³ As shown in Fig. 5e, the Cu2p XPS spectrum of the catalyst shows the peaks of Cu2p_{3/2} and Cu2p_{1/2} with binding energy at 934.0 eV and 953.7 eV, respectively, and that the spin energy separation between Cu2p_{3/2} and Cu2p_{1/2} is 19.7 eV, which is characteristic of Cu²⁺ species on the surface of the support.⁵⁴ Moreover, satellite peaks at 942.2 eV and 962.6 eV confirm the formation of CuO.⁵⁵

The H₂-TPR profile of the catalyst is shown in Fig. 6. It is clear that the main reduction appears in the temperature range of 100–250 °C, which can be ascribed to the reduction of CuO (Cu²⁺) to metallic Cu (Cu⁰), confirming the complete reduction of CuO during H₂ reduction process.⁵⁶ The broader peak at higher temperatures, *i.e.*, over 300 °C, is associated with the partial reduction of ZnO.⁵⁷

The catalytic testing of 15% CuZn/mesocarbon catalyst in CO₂ hydrogenation to methanol reaction was carried out in a temperature range of 225–300 °C and at a pressure of 15 bar. In the results in Fig. 7a, it is noticeable that the maximum space-time yield of methanol and CO₂ conversion are 498 mg g_{cat}^{−1} h^{−1} and 28.0 ± 2%, respectively, at a reaction temperature of 240 °C.

**Fig. 6** H₂-TPR profile of 15% CuZn/mesocarbon.**Fig. 7** Space-time yield of methanol and CO₂ conversion as a function of temperature (a), and space-time yield of methanol as a function of time-on-stream (b), using 15% CuZn/mesocarbon catalyst.

Further increasing the reaction temperature up to 300 °C, the performance in terms of both space-time yield of methanol and CO₂ conversion was found to decrease due to an exothermic effect.²⁴ Moreover, the space-time yield of methanol remained stable with a long time-on-stream as shown in Fig. 7b. Moreover, the average MeOH selectivity was found to be 94%, and the rest are CO and CH₄ as minor products. This implied that there are side reactions occurred competing with methanol formation. The possible mechanism of MeOH formation is believed to follow Arena *et al.*'s report⁵⁸ Briefly, CO₂ molecule is adsorbed at ZnO active site *via* C–O bonding, and simultaneously, H₂ is adsorbed at Cu⁰ sites and dissociated to 2 protons. Then, the proton will react with adsorbed CO₂ forming formate (HCOO) first and then HCOOH, H₂CO, H₃CO, and finally CH₃OH. The successive hydrogenation of the C atom will direct to the formation of CH₃OH, while the hydrogenation of the O atoms will weaken the C–O bond and direct to the formation of CO.⁵⁹

To confirm the structural stability of the spent catalyst, the XRD pattern in Fig. S1 (ESI[†]) can be used; this presents the same peak pattern of the fresh catalyst, attributable to high stability of the catalyst. In addition, as summarized in Table 2, this catalyst exhibits high catalytic performance compared with those in other previous published works,^{23,50,60–62} while using a low-cost and environmentally green chemical synthesis. Comparing to N-doped reduced graphene oxide aerogel,⁵¹ the PBZ derived mesocarbon can be prepared with lower-cost and more environmental-friendly process, while it gives a higher MeOH yield.

Table 2 Comparison of performance of carbon-supported catalysts in this work and previous work for CO₂ hydrogenation to methanol

Sample	Temperature (°C)	Pressure (bar)	STY of CH ₃ OH (mg _{MeOH} g _{cat} ⁻¹ h ⁻¹)	Ref.
15% CuZn/mesocarbon	250	15	498	This work
CuZn/N-rGO	250	15	424	23
CuZn/NrGOae-U	250	15	405	37
CuOZnOZrO ₂ Al ₂ O ₃ /rGO	240	20	310	60
Cu-ZrO ₂ /CNTs	260	30	84	61
PdZn/AC	250	30	28	62
PdZn/CNTs	250	30	37	62

4. Conclusions

In summary, PBZ-based mesocarbon material was introduced for the first time as the support of Cu-Zn catalyst used in the CO₂ hydrogenation to methanol. The mesocarbon support was successfully synthesized by benzoxazine solventless method followed by sol-gel method and carbonization to transform a self-formed mesoporous structure into mesoporous carbon. Moreover, this synthesis route has the advantages of reduced toxicity and low production cost, leading to providing a promising, environmentally friendly process. Furthermore, it is found that the 15% CuZn/mesocarbon catalyst shows the maximum space-time yield of methanol (498 mg g_{cat}⁻¹ h⁻¹) and CO₂ conversion (28 ± 2%) at a reaction temperature of 240 °C and pressure of 15 bar, resulting from the presence of nitrogen atoms leading to prevention of the agglomeration of metal and enhancement of the adsorption of CO₂, as well as facilitating the dissociation of H₂.

Conflicts of interest

There are no conflicts to declare.

Acknowledgements

This research was supported in part by the National Nanotechnology Center (NANOTEC), NSTDA, Ministry of Higher Education, Science, Research, and Innovation, through its program of Research Network of NANOTEC (RNN), by the Faculty of Engineering, Kasetsart University (research assistant scholarship for A. Chukchuan), and the Kasetsart University Research and Development Institute (KURDI).

Notes and references

- P. Friedlingstein, R. M. Andrew, J. Rogelj, G. P. Peters, J. G. Canadell, R. Knutti, G. Luderer, M. R. Raupach, M. Schaeffer, D. P. van Vuuren and C. Le Quéré, *Nat. Geosci.*, 2014, **7**, 709–715.
- F. A. Rahman, M. M. A. Aziz, R. Saidur, W. A. W. A. Bakar, M. R. Hainin, R. Putrajaya and N. A. Hassan, *Renewable Sustainable Energy Rev.*, 2017, **71**, 112–126.
- R. Barker, Y. Hua and A. Neville, *Int. Mater. Rev.*, 2017, **62**, 1–31.
- J. Gaede and J. Meadowcroft, in Carbon capture and storage demonstration and low-carbon energy transitions: explaining limited progress, ed. T. Van de Graaf, B. K. Sovacool, A. Ghosh, F. Kern and M. T. Klare, *The Palgrave Handbook of the International Political Economy of Energy*, Palgrave Macmillan UK, London, 2016.
- G. A. Olah, G. K. S. Prakash and A. Goeppert, *J. Am. Chem. Soc.*, 2011, **133**, 12881–12898.
- P. Su, K. Iwase, S. Nakanishi, K. Hashimoto and K. Kamiya, *Small*, 2016, **12**, 6083–6089.
- H. Nishihara, T. Hirota, K. Matsuura, M. Ohwada, N. Hoshino, T. Akutagawa, T. Higuchi, H. Jinnai, Y. Koseki, H. Kasai, Y. Matsuo, J. Maruyama, Y. Hayasaka, H. Konaka, Y. Yamada, S. Yamaguchi, K. Kamiya, T. Kamimura, H. Nobukuni and F. Tani, *Nat. Commun.*, 2017, **9**, 109.
- J. A. Mennel, H. Pan, S. W. Palladino and C. J. Barile, *J. Phys. Chem. C*, 2020, **124**, 19716–19724.
- G. A. Olah, *Angew. Chem., Int. Ed.*, 2005, **44**, 2636–2639.
- X. Niu, J. Gao, K. Wang, Q. Miao, M. Dong, G. Wang, W. Fan, Z. Qin and J. Wang, *Fuel Process. Technol.*, 2017, **157**, 99–107.
- C. Pirola, F. Galli, C. L. Bianchi, D. C. Boffito, A. Comazzi and F. Manenti, *Energy Fuels*, 2014, **28**, 5236–5240.
- T. Kropp, J. Paier and J. Sauer, *J. Catal.*, 2017, **352**, 382–387.
- X. Wang, R. Li, S. U. H. Bakhtiar, F. Yuan, Z. Li and Y. Zhu, *Catal. Commun.*, 2018, **108**, 64–67.
- J. Xu, X. Su, X. Liu, X. Pan, G. Pei, Y. Huang, X. Wang, T. Zhang and H. Geng, *Appl. Catal., A*, 2016, **514**, 51–59.
- T. Lunkenbein, F. Girgsdies, T. Kandemir, N. Thomas, M. Behrens, R. Schlögl and E. Frei, *Angew. Chem., Int. Ed.*, 2016, **55**, 12708–12712.
- M. Behrens, F. Studt, I. Kasatkin, S. Köhl, M. Hävecker, F. Abild-Pedersen, S. Zander, F. Girgsdies, P. Kurr, B.-L. Kniep, M. Tovar, R. W. Fischer, J. K. Nørskov and R. Schlögl, *Science*, 2012, **336**, 893–897.
- W. R. A. M. Robinson and J. C. Mol, *Appl. Catal.*, 1990, **60**, 73–86.
- S. D. Pike, A. García-Trenco, E. R. White, A. H. M. Leung, J. Weiner, M. S. P. Shaffer and C. K. Williams, *Catal. Sci. Technol.*, 2017, **7**, 3842–3850.
- A. Karelovic and P. Ruiz, *Catal. Sci. Technol.*, 2015, **5**, 869–881.
- F. Arena, G. Mezzatesta, G. Zafarana, G. Trunfio, F. Frusteri and L. Spadaro, *J. Catal.*, 2013, **300**, 141–151.
- B. An, J. Zhang, K. Cheng, P. Ji, C. Wang and W. Lin, *J. Am. Chem. Soc.*, 2017, **139**, 3834–3840.
- D. Großmann, A. Dreier, C. Lehmann and W. Grünert, *Appl. Catal., A*, 2015, **504**, 351–360.
- V. Deerattrakul, P. Dittanet, M. Sawangphruk and P. Kongkachuichay, *J. CO₂ Util.*, 2016, **16**, 104–113.
- V. Deerattrakul, P. Puengampholsrisook, W. Limphirat and P. Kongkachuichay, *Catal. Today*, 2018, **314**, 154–163.
- T. Takeichi, Y. Saito, T. Agag, H. Muto and T. Kawauchi, *Polymer*, 2008, **49**, 1173–1179.

- 26 Y. Liu, J. Chen, Y. Zhang, S. Gao, Z. Lu and Q. Xue, *J. Polym. Sci., Part B: Polym. Phys.*, 2017, **55**, 1813–1821.
- 27 R. Sasi Kumar, M. Ariraman and M. Alagar, *RSC Adv.*, 2014, **4**, 19127–19136.
- 28 N. P. Wickramaratne, J. Xu, M. Wang, L. Zhu, L. Dai and M. Jaroniec, *Chem. Mater.*, 2014, **26**, 2820–2828.
- 29 X. Xu, C. Song, J. M. Andresen, B. G. Miller and A. W. Scaroni, *Microporous Mesoporous Mater.*, 2003, **62**, 29–45.
- 30 A. Arenillas, K. Smith, T. C. Drage and C. E. Snape, *Fuel*, 2005, **84**, 2204–2210.
- 31 A. Arenillas, T. C. Drage, K. M. Smith and C. E. Snape, *J. Anal. Appl. Pyrolysis*, 2005, **74**, 298–306.
- 32 U. Thubsuang, H. Ishida, S. Wongkasemjit and T. Chaisuwan, *J. Math. Sci.*, 2014, **49**, 4946–4961.
- 33 H. Ishida and Y. Rodriguez, *Polymer*, 1995, **36**, 3151–3158.
- 34 V. Deerattrakul, W. Limphirat and P. Kongkachuichay, *J. Taiwan Inst. Chem. Eng.*, 2017, **80**, 495–502.
- 35 S. Gu, Z. Li, T. Miyoshi and S. C. Jana, *RSC Adv.*, 2015, **5**, 26801–26805.
- 36 T. Takeichi, T. Kano and T. Agag, *Polymer*, 2005, **46**, 12172–12180.
- 37 V. Deerattrakul, N. Yigit, G. Rupprechter and P. Kongkachuichay, *Appl. Catal., A*, 2019, **580**, 46–52.
- 38 Q. Lin, S. Dong, L. Qu, C. Fang and K. Luo, *J. Anal. Appl. Pyrolysis*, 2014, **106**, 164–170.
- 39 S. J. Gregg and K. S. W. Sing, *Adsorption, surface area and porosity*, Academic Press, London, 2nd edn, 1982.
- 40 W. Ahmad, F. L. Chan, A. Hoadley, H. Wang and A. Tanksale, *Appl. Catal., B*, 2020, **269**, 118765.
- 41 N. Mahata, O. S. G. P. Soares, I. Rodríguez-Ramos, M. F. R. Pereira, J. J. M. Órfão and J. L. Figueiredo, *Appl. Catal., A*, 2013, **464–465**, 28–34.
- 42 P. Iamprasertkun, A. Krittayavathananon and M. Sawangphruk, *Carbon*, 2016, **102**, 455–461.
- 43 D. Guo, R. Xin, Y. Wang, W. Jiang, Q. Gao, G. Hu and M. Fan, *Microporous Mesoporous Mater.*, 2019, **279**, 323–333.
- 44 V. C. Tung, M. J. Allen, Y. Yang and R. B. Kaner, *Nat. Nanotechnol.*, 2009, **4**, 25–29.
- 45 H. Wang, H. Peng, G. Li and K. Chen, *Chem. Eng. J.*, 2015, **275**, 160–167.
- 46 P. Iamprasertkun, W. Hirunpinyopas, A. Keerthi, B. Wang, B. Radha, M. A. Bissett and R. A. W. Dryfe, *J. Phys. Chem. Lett.*, 2019, **10**, 617–623.
- 47 R. Sasi Kumar, M. Ariraman and M. Alagar, *RSC Adv.*, 2015, **5**, 23787–23797.
- 48 H. Fang, L. Zhao, W. Yue, Y. Wang, Y. Jiang and Y. Zhang, *Electrochim. Acta*, 2015, **186**, 397–403.
- 49 D. Hulicova-Jurcakova, M. Seredych, G. Q. Lu and T. J. Bandosz, *Adv. Funct. Mater.*, 2009, **19**, 438–447.
- 50 S. Ganesan, N. Leonard and S. C. Barton, *Phys. Chem. Chem. Phys.*, 2014, **16**, 4576–4585.
- 51 W. Fan, Y.-E. Miao, Y. Huang, W. W. Tjiu and T. Liu, *RSC Adv.*, 2015, **5**, 9228–9236.
- 52 X. Ma, L. Li, S. Wang, M. Lu, H. Li, W. Ma and T. C. Keener, *Appl. Surf. Sci.*, 2016, **369**, 390–397.
- 53 I. G. Morozov, O. V. Belousova, D. Ortega, M. K. Mafina and M. V. Kuznetsov, *J. Alloys Compd.*, 2015, **633**, 237–245.
- 54 J. Morales, J. P. Espinos, A. Caballero, A. R. Gonzalez-Elipe and J. A. Mejias, *J. Phys. Chem. B*, 2005, **109**, 7758–7765.
- 55 O. Akhavan, R. Azimirad, S. Safa and E. Hasani, *J. Mater. Chem.*, 2011, **21**, 9634–9640.
- 56 Y. Zhang, C. Chen, X. Lin, D. Li, X. Chen, Y. Zhan and Q. Zheng, *Int. J. Hydrogen Energy*, 2014, **39**, 3746–3754.
- 57 A. García-Trenco and A. Martínez, *Catal. Today*, 2013, **215**, 152–161.
- 58 F. Arena, G. Italiano, K. Barbera, S. Bordiga, G. Bonura, L. Spadaro and F. Frusteri, *Appl. Catal., A*, 2008, **350**, 16–23.
- 59 X. Cui, W. Yan, H. Yang, Y. Shi, Y. Xue, H. Zhang, Y. Niu, W. Fan and T. Deng, *ACS Sustainable Chem. Eng.*, 2021, **9**, 2661–2672.
- 60 Y. J. Fan and S. F. Wu, *J. CO₂ Util.*, 2016, **16**, 150–156.
- 61 G. Wang, L. Chen, Y. Sun, J. Wu, M. Fu and D. Ye, *RSC Adv.*, 2015, **56**, 45320–45330.
- 62 X. L. Liang, X. Dong, G. D. Lin and H. B. Zhang, *Appl. Catal., B*, 2009, **88**, 315–322.